

Limits on the Size and Orbit Distribution of Main Belt Comets

S. Sonnett, J. Kley, R. Jedicke

*Institute for Astronomy, University of Hawaii at Manoa, 2680 Woodlawn Drive,
Honolulu, HI, 96822*

J. Masiero

Jet Propulsion Laboratory, M/S 321-520, 4800 Oak Grove Drive, Pasadena, CA, 91109

Abstract

The first of a new class of objects now known as main belt comets (MBCs) or “activated asteroids” was identified in 1996. The seven known members of this class have orbital characteristics of main belt asteroids yet exhibit dust ejection like comets. In order to constrain their physical and orbital properties we searched the Thousand Asteroid Light Curve Survey (TALCS; Masiero *et al.*, 2009) for additional candidates using two diagnostics: tail and coma detection. This was the most sensitive MBC survey effort to date, extending the search from MBCs with $H \sim 18$ ($D \sim 1$ km) to MBCs as small as $H \sim 21$ ($D \sim 150$ m).

We fit each of the 924 objects detected by TALCS to a PSF model incorporating both a coma and nuclear component to measure the fractional contribution of the coma to the total surface brightness. We determined the significance of the coma detection using the same algorithm on a sample of null detections of comparable magnitude and rate of motion. We did not identify any MBC candidates with this technique to a sensitivity limit on

the order of cometary mass loss rate of about 0.1 kg/s.

Our tail detection algorithm relied on identifying statistically significant flux in a segmented annulus around the candidate object. We show that the technique can detect tail activity throughout the asteroid belt to the level of the currently known MBCs. Although we did not identify any MBC candidates with this technique, we find a statistically significant detection of faint activity in the entire ensemble of TALCS asteroids. This suggests that many main belt asteroids are active at very low levels.

Our null detection of MBCs allows us to set 90% upper confidence limits on the number distribution of MBCs as a function of absolute magnitude, semimajor axis, eccentricity, and inclination. There are $\lesssim 400000$ MBCs in the main belt brighter than $H_V = 21$ (~ 150 -m in diameter) and the MBC:MBA ratio is $\lesssim 1:400$.

We further comment on the ability of observations to meaningfully constrain the snow line's location. Under some reasonable and simple assumptions we claim 85% confidence that the contemporary snow line lies beyond 2.5 AU.

Keywords: Asteroids, Astrobiology, Comets

1. Introduction

The classical view of comets as icy conglomerations and asteroids as chunks of rock has been supplanted in the last decade by the realization that a population of objects exists between the two traditional extremes — comets are dirty iceballs and asteroids are icy dirtballs with the relative contribution and morphological structure of the ice and rock giving rise to the

classical views of each object. Thus, in the classical view, asteroids always exhibit bare nuclei photometric properties (Jewitt, 2008) while comets are characterized by a transient atmosphere and/or tail (Jewitt *et al.*, 2009). The early compositional distinction between asteroids and comets was further supported by the apparent bimodality in their orbit distributions — the known asteroids had nearly circular orbits confined to the torus of objects between Mars and Jupiter while the known comets had highly eccentric orbits taking them beyond Jupiter, Neptune and even out to the Oort Cloud¹. The modern view was ushered in by the discovery of comet-asteroid transition objects. In the ensemble of known small bodies there exist comets with asteroidal dynamical properties (*e.g.*, Chamberlin *et al.*, 1996; Fernandez *et al.*, 2005), asteroids on cometary orbits (Binzel *et al.*, 1993; Fernandez *et al.*, 2005), and Damocloids (inactive comets with dynamical properties of Halley-family and long-period comets; Jewitt, 2005).

This work focuses on those objects that appear to be comets — their morphology being consistent with a cometary nature in the sense that they exhibit comae or tails — but have asteroid-like orbits embedded in the main belt of asteroids. To this end, we have performed a well-characterized search for low-level cometary activity amongst a sample of nearly 1000 asteroids from TALCS (Masiero *et al.*, 2009).

The first cometary main belt object, now known as a main belt comet (MBC) or an “activated asteroid”, was identified in observations of what is now known as Comet 133P/Elst-Pizarro (hereafter, EP; Elst *et al.*, 1996). It

¹Asteroids and comets may be distinguished by their Tisserand parameter with respect to Jupiter (T_J) - comets typically have $T_J < 3.0$ while asteroids generally have $T_J > 3.0$.

exhibits recurrent dust ejection over several weeks or months (Boehnhardt *et al.*, 1996). Hsieh & Jewitt (2006b) described a detailed study of EP and showed that its cometary activity is correlated with heliocentric distance. Hsieh *et al.* (2010) then showed that EP’s activity is also seasonal — there is a region on the surface that becomes active when it experiences its local ‘summer’. They then explored two dynamical scenarios that might explain EP’s transient cometary activity and its orbital characteristics embedded in the outer region of the main belt.

Their first scenario is that EP began as a Jupiter family comet (JFC) but migrated inward via both non-gravitational (*i.e.*, cometary outgassing) and gravitational influences. However, none of the simulations of the dynamical evolution of JFC test particles under solely gravitational influences result in an inclination as low as EP’s (Fernandez *et al.*, 2002). Ipatov *et al.* (2007) showed that non-gravitational forces can be strong enough to bring EP to its contemporary orbit, but its current activity level is unlikely to have produced enough of a perturbation to do so (Hsieh & Jewitt, 2006b).

Alternatively, Hsieh & Jewitt (2006b) suggested that EP could be the first of a large number of asteroids containing a reservoir of ice beneath their surface. This scenario is consistent with thermal evolution models of large asteroids that escaped primordial heating and with evidence of aqueous alterations in meteorites (Grimm & McSween 1989; Fanale & Salvail 1989; Prialnik & Rosenberg 2009). Furthermore, Prialnik & Rosenberg (2009) show that crystalline water ice from the time of their formation can survive within the interior of outer main belt asteroids. The MBCs were not discovered earlier because they are rare and their activity is both weak and/or transient.

The release of buried volatiles requires some triggering event like an impact (even a small one) or the warming effect of perihelion passage (Jones *et al.* 1990; Scott & Krot 2005; Hsieh *et al.* 2004; Capria *et al.* 2010), and their detection requires regular monitoring of a large sample of asteroids. These conditions were not met until the advent of modern wide-field asteroid surveys.

The origin of EP and other MBCs is of interest in planetary formation in part because they offer an opportunity to identify the location of the ‘snow line’ — the heliocentric distance at which ices condensed in the early solar system (*e.g.*, Sasselov & Lecar 2000; Kennedy & Kenyon 2008). MBCs should only be found outside the snowline assuming that there has been only limited heliocentric mixing of the asteroids. Furthermore, the existence and properties of a large sample of MBCs will provide tests of asteroid thermal models, common origin scenarios, and dispersion mechanisms. For example, considering significant instead of limited heliocentric mixing, MBC studies can provide hints on how this mechanism functioned in the early solar system environment.

In an attempt to identify more MBCs when only two were known, Hsieh & Jewitt (2006a) conducted a targeted survey of about 300 asteroids in the outer main belt and found one more in the orbital region of the other two MBCs. All three have similar orbit characteristics with $3.156 \leq a \leq 3.196$ AU, $0.165 \leq e \leq 0.253$, and $0.24^\circ \leq i \leq 1.39^\circ$ (Table 1). Two of the three belong to the Themis dynamical family while the third (P/Read) has an eccentricity slightly higher than the Themis family’s upper limit. Nesvorny *et al.* (2008) suggest that P/Read used to be a Themis family member that

is dynamically evolving away from its parent cluster. Hsieh & Jewitt (2006b) estimated that the MBC:MBA ratio is $\sim 1:300$ and measured MBC mass loss rates in the range of $0.01 - 1.5$ kg/s compared to typical cometary mass loss rates of $\sim 10^{-3} \lesssim \dot{M}$ (kg/s) $\lesssim 10^3$ (*e.g.*, Lamy *et al.*, 2004). Since then, four additional MBCs have been discovered outside the vicinity of the original three MBCs with two of them located in the middle belt. Some characteristics of all seven objects are provided in Table 1. For at least two of the MBCs in Table 1, the observed activity is most likely the result of asteroid collisions and be devoid of recurrent activity characteristic of comets (596 Scheila and P/2010 A2/Linear; Jewitt *et al.*, 2010; Snodgrass *et al.*, 2010; Jewitt *et al.*, 2011).

One of the major difficulties in searching for new MBCs and mapping their distribution is detecting and quantifying their subtle cometary nature. Several techniques have been employed in the past to identify low activity comets; most were designed to search for faint comae.

One method is to identify optical emission lines of typical cometary gases (*e.g.*, Cochran *et al.*, 1986). Detecting these faint spectroscopic features (*e.g.*, the CN(0-0) and C₂ bands at 388nm and 517nm, respectively) requires high S/N objects and a relatively large amount of telescope time for each object making it difficult to employ on a large sample of main belt candidates.

Another method to search for cometary activity requires multiple photometric observations of the targets over a wide range of phase angles to identify non-asteroidal photometric behavior. The flux of scattered light off an asteroidal target is proportional to the product of its phase function, the inverse square of its heliocentric distance, and the inverse square of its geo-

centric distance. Failure of the target’s photometric profile to follow this behavior suggests a variable coma (Hartmann *et al.*, 1990).

Speckle interferometry has also been used to distinguish comae but it is limited to only the brightest objects with $m_V \leq 14$, limiting this process to the largest $\sim 28,000$ asteroids or $\sim 7\%$ of the known main belt objects (Drummond *et al.* 1989; Bowell 2007). The process also requires considerable telescope time for each target.

Gilbert & Wiegert (2009) attempted to identify main-belt comets morphologically using the expected FWHM-broadening of the target PSF perpendicular to the direction of motion. In a follow-up paper, Gilbert & Wiegert (2010) identified one object that may be either an MBC candidate or a regular comet and set an upper limit on the number of MBCs in the main belt of 40 ± 18 to a limiting size of ~ 1 km (absolute magnitude $H \sim 16$).

To identify MBC candidates Luu & Jewitt (1992) compared MBC candidates to stellar profiles with the expectation that a wider asteroidal profile would indicate the presence of coma. We adopted and refined this method in our search for new MBCs amongst the asteroids identified in TALCS (Masiero *et al.*, 2009). That survey identified 924 asteroids with multiple $S/N > 5$ detections of each object using the CFHT’s MegaPrime camera. Our goal was to carefully examine each TALCS asteroid for low-level cometary activity and determine the MBC number distribution as a function of semi-major axis (a), eccentricity (e), inclination (i), and absolute magnitude (H) or diameter (D). We used two techniques to identify cometary activity around otherwise asteroidal objects: one for tail detection and another for comae detection. We then corrected for observational selection effects and derived

limits on the unbiased orbit and number distribution of the MBCs.

2. Observations

We obtained a large set of asteroid detections from TALCS (Masiero *et al.*, 2009) which was designed to measure light curve properties of ~ 1000 Main Belt asteroids with diameters in the range $0.5 \text{ km} < D < 10 \text{ km}$. The survey was conducted with the Canada-France-Hawaii Telescope's MegaPrime camera whose image plane is instrumented with an array of 36 CCDs that each contain 2048×4612 pixels. With a pixel scale of $0.185''/\text{pixel}$ MegaCam covers a field of $\sim 1^\circ \times 1^\circ$. TALCS used the g' and r' filters with integration times of 20 and 40 seconds yielding $5\text{-}\sigma$ detections at about 23.3 and 24.3 magnitudes respectively (Fukugita *et al.*, 1996).

Figure 1 shows that the number distribution of TALCS objects is well-sampled through the main belt. In the inner belt ($a < 2.50 \text{ AU}$), middle belt ($2.501 < a < 2.824 \text{ AU}$) and outer belt ($a > 2.824 \text{ AU}$) there were 286, 287 and 352 objects respectively. It is unsurprising that the distribution of TALCS objects in semi-major axis and eccentricity matches that of the known objects because in these elements the TALCS survey is similar to most other asteroid surveys. TALCS is biased against high-inclination objects (see Figure 1C) because it surveyed a relatively small region on the ecliptic for a short period of time. The median $H \sim 18$ corresponds to $\sim 1 \text{ km}$ in diameter (Bowell 2007). This size range is well suited to a MBC search based on the known objects listed in Table 1.

3. The Search for Tails

The three MBCs observed by Hsieh & Jewitt (2006a) had tails or dust trails but weak or nonexistent comae. This observation motivated us to develop an algorithm to identify MBC tails but the problem is complicated by the facts that they 1) are much fainter than typical cometary tails, 2) are transient and may appear or disappear during the course of the TALCS survey and 3) may appear at any position angle and change their orientation from night-to-night. Our tail detection algorithm needed to be robust against all these possibilities.

3.1. Method

Our tail identification strategy was to divide an annulus of sky around each detection into eighteen 20° truncated pie segments (Figure 2) and search for an anomalously bright segment, comparing the result to a set of comparison stars. Using segments is preferable to summing the light in the entire annulus because the S/N of a tail detection increases as the square root of the number of segments as long as the tail falls into only one segment. The benefit of noise suppression dominates even though the number of opportunities for a false detection scales with the number of segments. This technique is an analog to a traditional matched detection kernel using a detection region that mimics the shape of the detected object.

We used a detection annulus extending from $4''$ to $8''$ from the asteroid. For an asteroid at a geocentric distance of ~ 2 AU, this is equivalent $\sim 6000 - 12000$ km from the nucleus. To reduce contamination of the MBC candidate by other faint astronomical sources in the image we rejected as-

teroid and comparison star detections with a neighboring object within $11''$. A larger annulus increases the S/N only modestly but greatly increases the number of images rejected because of neighboring objects. The diameter of the inner edge of the annulus was selected to avoid most of the light from the target's PSF. Trailing is not an issue because the inner radius of the detection aperture is much larger than the typical trailing distance of $\lesssim 0.3''$.

For each image (detection) i of each asteroid we determine the flux of the brightest annular segment and repeat the procedure for nearby stars in the same image with fluxes similar to the asteroid. Next, we rank the brightest segment of the asteroid among the brightest segment of the stars with a cumulative parameter f_i . For example, $f_i = 0.1$ would mean that the brightest segment for asteroid detection i is in the top 10% of all the brightest segments of the comparison stars. Under the null hypothesis of no MBC activity the values of f_i are uniformly distributed between 0 and 1. In the presence of MBC activity there is an excess of detections having small values of f_i .

A compelling feature of this method is that the null hypothesis distribution of f_i is well defined, non-parametric, and immune to many types of systematics. The set of f_i that are used to combine data across observing nights are independent of variations in observing conditions and concentrations of background contamination (*e.g.*, unresolved galaxies) because it is calibrated with stars observed under the same conditions within the same image.

3.2. Sensitivity

The sensitivity of any search method depends on the strength of the signal (in our case, the tail) relative to random background noise and systematic background artifacts. To test the sensitivity of our tail identification method we performed a Monte Carlo simulation using simplified Gaussian statistics to generate a set of f_i with signal strengths expressed as a fraction of the standard deviation of counts over the entire annulus. We then compared the set to the uniform null hypothesis. We assumed 50 identical observations per object and 100 calibration stars. In the actual data, we have 38 ± 17 valid measurements of each asteroid, and each measurement uses 54 ± 19 calibration stars within ± 1 magnitude of its object.

We repeated the procedure for $N_{\text{seg}} = 1, 9, 18,$ and 36 segments corresponding to angular widths of $360^\circ, 40^\circ, 20^\circ,$ and $10^\circ,$ respectively. For each N_{seg} we conducted 1000 trials and computed the median Kolmogorov-Smirnov ² probability with which a tail of the given strength is recovered. For comparison, we also computed the recovery strength for simple additive and median stacking of the images assuming no systematic noise and perfect tail alignment among images.

Figure 3 shows that our 18 segment scheme can detect tails at the $p = 10^{-5}$ significance if they have a tail S/N of $\gtrsim 0.45$. Increasing N_{seg} allows the detection of fainter tails but we chose $N_{\text{seg}} = 18$ as a compromise between

²The Kolmogorov-Smirnov test is a standard non-parametric statistical test comparing two distributions based on the maximum difference between their cumulative distributions. A low probability p is derived if it is unlikely that the two distributions are drawn from the same underlying distribution.

sensitivity and the ability to detect wide tails.

We selected a 10^{-5} significance as our threshold detection level because a given asteroid will achieve this level by chance only 1 time out of 10^5 , so our ~ 1000 asteroid sample has a 1 in 100 chance of containing a value this large. In other words, a signal at this level for an asteroid in our sample would provide roughly 100 to 1 evidence for MBC activity if we believe that there is a good chance that there is one MBC in our sample.

Additive or median stacking of the images followed by selecting the brightest segment can detect fainter tails than our approach but these techniques are sensitive to image artifacts as well as tail rotation and transience. Even though additive stacking is the most sensitive method in Fig. 3, it would not suppress image artifacts and we do not consider it a viable option. Relative to median stacking our method trades a factor of two in sensitivity in the ability to connect images obtained under different observing conditions. It permits the tail to rotate in position angle between images and allows for the possibility that activity ceases in some images (in which case median stacking could lose the signal entirely).

We tested the sensitivity of our method on real data using MBC images obtained with the University of Hawaii (UH) 2.2-m telescope (Hsieh & Jewitt 2006a). For the three known MBCs there are 17 to 25 30s exposures totaling 1.5 to 2.1 hours of exposure time — the equivalent of forty minutes cumulative exposure on the larger CFHT telescope used for TALCS. Hence, the total exposure time for the three MBCs is similar to that of a CFHT TALCS object imaged on a hundred 30s exposures. The shorter TALCS/CFHT exposure, with four times less signal than the 2.2-m data, will suppress the S/N of the

brightest segment by a factor of 2 in any individual exposure relative to the UH 2.2-m data. Thus, the UH 2.2-m data set allows the identification of tails that are half as bright as the CFHT/TALCS data but the larger number of exposures in TALCS allows a more robust rejection of the null hypothesis uniform f distribution.

Figure 4 shows the f distributions produced by our method for three known MBCs. The number of entries in the histograms are considerably smaller than the number of exposures because our stringent background rejection criteria removed many images from the sample. In each case, the Kolmogorov-Smirnov probability p_{KS} is much smaller than unity, strongly ruling out the null hypothesis. Even the faintest MBC, 176P/Linear, for which a tail is invisible to the eye in individual exposures, shows a tail detection in each frame using our polar segment method. Moreover, from the inset circular histograms it is evident that the brightest segment consistently points in the same direction providing a second signature of MBC activity.

Table 2 provides two measures of the technique’s sensitivity for three known MBC tails: in terms of 1) the tail flux as a fraction of the object’s central flux and 2) the g' magnitude within the brightest detection segment. We used the published R magnitudes for the three MBCs (Hsieh & Jewitt, 2006a) and the color transformations of Jester *et al.* (2005) to calculate g' . Two of the MBCs have a total tail magnitude in the detection aperture of $g \approx 23$ while the third is about one magnitude brighter. Thus, the technique is capable of detecting tail activity corresponding to a few percent of the brightness of the object itself.

Finally, we measured our ability to recover artificial tails inserted into the

TALCS data. Figure 5 shows that tails with $g' = 23.12$ in the detection slice, comparable to the tail brightness of the fainter known MBCs, would almost always be recovered with $p_{\text{KS}} \ll 10^{-10}$. Since any detection with $p_{\text{KS}} < 10^{-5}$ in our sample of $\sim 10^3$ objects is indicative of genuine MBC activity at the 99% confidence level, this technique is clearly sensitive to MBC activity at the level of the known objects. Figure 5C shows that tails that are only 0.5 magnitudes fainter than 23.12 would not be reliably detected. Nevertheless, the presence of fainter tails is detectable over the ensemble as a whole and their magnitude is recovered correctly as shown in Figure 5D.

4. The Search for Comae

Comets may exhibit a coma despite having a weak or undetectable tail (*e.g.*, 49P/Arend-Rigaux, Millis *et al.*, 1988) but detecting the contribution of faint coma to the nuclear PSF is difficult. Thus, we developed a technique to identify faint comae by expanding upon the work of Luu & Jewitt (1992). For each TALCS object n , we fit a stacked image of all detections for the object (F_n) to a linear combination of a target-specific asteroid PSF model ($F_{A,n}$) and target-specific isotropic coma PSF model ($F_{C,n}$):

$$F_n(i, j) = f_a F_{A,n}(i, j) + f_c F_{C,n}(i, j) . \quad (1)$$

where (i, j) is the pixel in the stacked image. Modeling the target flux is necessarily imprecise because 1) the PSF varies from night-to-night and across the field-of-view of the wide-field CFHT MegaPrime camera, 2) asteroids move during the course of the exposures producing trails of different lengths for each object and even for the same object in different images because they were taken up to two weeks apart, and 3) not all comae are isotropic.

The mass loss rate (\dot{M}) from a comet is given by (Luu & Jewitt, 1992)

$$\frac{\dot{M}}{\text{kg/s}} = 10^{-3} \pi \eta \frac{\bar{a}}{\mu\text{m}} \frac{\rho}{\text{kg m}^{-3}} \left(\frac{r}{\text{km}} \right)^2 \frac{\text{arcsec}}{\phi} \frac{\text{AU}}{\Delta} \sqrt{\frac{\text{AU}}{R}} , \quad (2)$$

where ρ is the grain density, \bar{a} is the average expelled grain radius, η is the ratio of the flux density of the coma to that of the nucleus, r is the radius of the target, ϕ is the photometric diaphragm, and R and Δ are the heliocentric and geocentric distances, respectively. We expect the particles ejected from MBCs are small - similar to cometary material with grain radii of $0.5 \mu\text{m}$, and we expect that they have densities typical of solid rocky material (Britt *et al.*, 2002; Luu & Jewitt, 1992). We therefore used $0.5 \mu\text{m}$ for grain radius and 3000 kg/m^3 for grain density in our calculations. From eq. 1, $\eta \equiv \frac{f_c}{f_a}$, and thus we can determine the mass loss rate for the TALCS objects.

We calculated each objects's heliocentric and geocentric distances from their orbits and estimate their radii using (Lamy *et al.*, 2004):

$$r \sim \frac{673 \times 10^{-H/5}}{\sqrt{A}} ,$$

where A is the geometric albedo. While TALCS did obtain photometry in two different filters for most of the targets the S/N was not sufficient to measure accurate colors for most objects (from which we could have assumed a taxonomic type and albedo). Therefore, we resorted to assigning a heliocentric distance-dependent albedo: $A = 0.134/0.103/0.076$ for objects in the inner/middle/outer main belt bounded by $2.064 \text{ AU} < a \leq 2.501 \text{ AU}$, $2.501 \text{ AU} < a \leq 2.824 \text{ AU}$, and $2.824 \text{ AU} < a \leq 3.277 \text{ AU}$, respectively (Jedicke & Metcalfe 1998; Klacka 1992).

4.1. Method

Figure 6 provides a schematic representation of how we produced the three components of our linear fits in eq. 1: 1) the stacked target object images, $F_n(i, j)$, to which we fit our models, 2) the synthetic asteroid models specific to each object, $F_{A,n}(i, j)$, that incorporate the same PSF, trailing and stacking as the target objects, and 3) the synthetic coma models, $F_{C,n}(i, j)$, that, again, incorporate the same PSF, trailing and stacking as the target objects.

4.1.1. Constructing the Stacked Target Image: $F_n(i, j)$

We began by extracting 200×200 pixel ($37'' \times 37''$) thumbnail images (hereafter “thumbnails”) for each target object n from each image m . The thumbnail is large enough to encompass background and a broad coma profile but also small enough to exclude most field stars. We median-stacked thumbnails of each background-subtracted flux-normalized object from images with $\leq 0.8''$ seeing as determined by nearby stellar profiles. The stacking was performed with sub-pixel offsets when centroiding the objects. We combined g' and r' images because our concerns are with a morphology that would manifest itself similarly in both bands. The background was assumed to be the median of all pixels in the thumbnail excluding those within $3''$ of the target’s center and was subtracted from each raw image. Since each target object appeared in multiple images under different seeing conditions and moving at slightly different rates each night the stacked object images had complicated PSFs.

4.1.2. *Constructing the asteroid model: $F_{A,n}(i, j)$*

We retrieved thumbnails for five nearby bright but unsaturated stars (10,000–50,000 ADU) for each object in each image (the median object flux being $\sim 2,500$ ADU). We then background-subtracted, flux-normalized, and median-combined the field star thumbnails in a fashion parallel to §4.1.1 to produce stacked star images $F_{S,n,m}$ to be used as PSF models for point sources specific to each TALCS object n in each image m . Constructing models from nearby field stars in this way maximized the similarities between the model and target PSFs’ morphological properties. Then, since the asteroids moved during each ~ 30 second exposure at rates that may have changed slightly from night to night, we artificially trailed the stacked star image ($F_{S,n,m}$) at the corresponding object’s rate of motion on a night-by-night basis to create an object-specific synthetic asteroid PSF.

To create the trailed PSFs we created $2N + 1$ shifted sub-images ($F_{S,n,m,k}$ with $-N \leq k \leq N$) of the stacked stars. The shift in pixels for each sub-image k is given by:

$$\begin{aligned} \Delta x_k &= \frac{k}{2N} \frac{1}{s} \frac{\Delta \alpha}{\Delta t} \\ \Delta y_k &= \frac{k}{2N} \frac{1}{s} \frac{\Delta \delta}{\Delta t}, \end{aligned}$$

where the pixel scale $s = 0.185''/\text{pixel}$ and we used $N = 5$ (*i.e.*, 11 sub-images). We need not consider cross terms because the CFHT MegaCam (x, y) axes are precisely aligned with (RA,Dec)=(α, δ) but we did take into account the $\cos(\delta)$ term for the motion in RA. The flux in each shifted stellar profile thumbnail ($F_{S,n,m,k}$) was then combined such that the flux in pixel (i, j) in the trailed, unnormalized asteroid model thumbnail ($F'_{A,n,m}$) for ob-

ject n in image m is

$$F'_{A,n,m}(i, j) = \frac{1}{2N + 1} \sum_k F_{S,n,m,k}(i, j) .$$

$F'_{A,n,m}$ was then normalized by its total flux within a $2.0''$ radius of the center to create the synthetic asteroid model ($F_{A,n,m}$) specific to each TALCS object and image. The models were then median-combined to sub-pixel accuracy across the images with seeing $< 0.8''$ and normalized to create a synthetic asteroid model specific to each TALCS object, $F_{A,n}$.

4.1.3. Constructing the Coma Model: $F_{C,n}(i, j)$

We also constructed one synthetic coma model ($F_{C,n}$) per TALCS object n using a method similar to the construction of the asteroid model (see §4.1.2). We convolved a spherically symmetric r^{-1} coma profile with each synthetic asteroid model before stacking ($F_{A,n,m}$) to create an unnormalized, image- and object- specific coma model $F'_{C,n,m}$. These models were then normalized by the total flux within the central $2.0''$ radius, median-combined across images as for the stacked TALCS objects themselves, and then once again normalized to produce the final object-specific coma model, $F_{C,n}$.

4.1.4. Fitting the Models

Fitting the stacked target object image to the linear combination of the stacked asteroid and coma models in eq. 1 requires an error model for the image(s). The photometric error ($E_{n,m}(i, j)$) on each pixel of $F_{n,m}$ — the normalized thumbnail for each TALCS detection before median combining — is the square root of the raw photon count including the background, normalized by the total flux from the background-subtracted image. We

then median-combined $E_{n,m}(i, j)$ using only those images m for which the seeing was $\leq 0.8''$ (as with the construction of the stacked target images and their asteroid and coma models) to produce $\tilde{E}_n(i, j)$. The error on each pixel of the stacked target object image is then:

$$E_n(i, j) = \frac{1.253}{N(i, j)} \tilde{E}_n(i, j) ,$$

where a standard factor of 1.253 is included to account for combining the median rather than the mean of the images and $N(i, j)$ is an integer array of the number of images included in the stack at each pixel. $N(i, j)$ is pixel-dependent because centroid shifting in the stack causes the thumbnails from different images to not overlap perfectly. A parallel method was used to determine errors for the synthetic asteroid and coma model images, $E_{A,n}(i, j)$ and $E_{C,n}(i, j)$, respectively.

The fitting algorithm assumes that the model, the right hand side of the equation, is error-free. We incorporated all the error into our stacked target object image as

$$E'_n(i, j) = \sqrt{E_n^2(i, j) + E_{A,n}^2(i, j)} .$$

The coma model's contribution to the error, $E_{C,n}(i, j)$, is negligible because it is a convolution of a perfectly symmetric, error-free model.

4.1.5. Dealing with Systematics

Despite the care devoted to creating customized PSF models for each object we found that our resulting formal errors on the fits to the stacked asteroid thumbnails could not compensate for all the systematic problems to the technique. *i.e.*, the formal errors on the derived f_c values suggested that a large fraction of the objects had significant coma and mass loss rate

despite there being no obvious visually detectable coma. Instead, like the tail detection method described above, we resorted to using a ranking method. Ranking statistics are more robust than parametric statistics because they do not assume any properties of the data (*e.g.*, Gaussian PSFs). Ranking each TALCS object’s coma fraction requires a set of similar objects that have no coma. We constructed the coma-free asteroid comparisons in the manner described below.

First, we defined a metric Z to quantify the similarity between 1) a target stacked asteroid image with magnitude \tilde{m} and rates of motion in the x and y direction of \tilde{x} and \tilde{y} respectively and 2) detections of other asteroids (k) with magnitude $m_{k,i}$ and rates of motion $\dot{x}_{k,i}$ and $\dot{y}_{k,i}$ in image i :

$$Z_{k,i}^2 = \frac{(m_{k,i} - \tilde{m})^2}{a^2} + \frac{(\dot{x}_{k,i} - \tilde{x})^2}{(b/2)^2} + \frac{(\dot{y}_{k,i} - \tilde{y})^2}{(b/2)^2},$$

The values of a and b were determined empirically to be the inverse of the limit at which PSFs of different magnitudes and trailing rates were similar enough to combine ($a = 0.2$ differential magnitudes and $b = 0.25$ pixels).

We then compiled a list of the N^2 smallest Z values for each stacked target asteroid where N is the number of frames that were used to construct the stacked target image and randomly selected N frames from these closest matches such that no more than 20% of the frames came from the same TALCS object and there were no duplicates. Combining the randomly-selected comparison frames renders a stacked image comparable to that of the target and absent of any coma unless more than 20% of the main belt asteroids with $H < 21$ display comae (which is highly unlikely given the rate of discovery for these sizes; Hsieh & Jewitt 2006b; Gilbert & Wiegert 2009). We call each of the generated stacked no-coma images a ‘null-image’

and could create as many null-images as necessary for each stacked target asteroid.

Then, to quantify the significance of the derived f_c for each stacked target asteroid we computed h , the percentile under which the target's f_c falls compared to the null-images (see §5.2 for a detailed discussion of h). In the absence of coma the distribution of h -values for a stacked asteroid image should be uniform.

4.2. Sensitivity

To determine the mass loss rate sensitivity of our coma detection method we generated 10,000 null-images each at magnitudes between 17 and 23 and at three heliocentric distances of $R = 1.6, 2.6, 3.6$ AU with corresponding geocentric distances of $\Delta = R - 1$. For each set of null-images we used the coma fitting procedure described above to determine f_c and used the 10th largest f_c from each set ($f_{c,limit}$) to represent the $p = 0.001$ statistical significance level - *i.e.*, there is a 1 in 1000 chance that a random stacking of assorted randomly chosen asteroids with mutually similar magnitudes and trailing rates) would produce $f_c > f_{c,limit}$. Then we converted $f_{c,limit}$ to a flux (or coma apparent magnitude) from which we derived a mass loss rate using Equation 2. Figure 7 shows the f_c $p = 0.001$ coma fraction (top) and the corresponding mass loss sensitivity limit (bottom) as a function of magnitude for the three values of R . For $R = 2.6$ AU, our sensitivity limit is typically better than 0.1 kg s^{-1} , although it varies by over an order of magnitude between $R = 3.6$ AU and 2.6 AU. Thus, our coma identification technique is sensitive to mass loss rates comparable to the known MBCs listed in Table 1.

5. Results & Discussion

5.1. Tail Search

Figure 8 shows the results of applying our segmented annulus tail detection technique described in §3 to all the asteroids in the TALCS data set. The strongest detection is at the KS probability level $p = 2.9 \times 10^{-4}$ which is expected to randomly occur about one third of the time in a sample of nearly 1000 asteroids. We conclude that we find no evidence of MBC tail activity in any individual asteroid within the TALCS data set. This result may not be surprising because half the TALCS sample has $H_v > 17.7$ and thus are smaller than the smallest known MBC. Smaller objects may be less likely to have tails because there is less volume to store the volatiles and less regolith to protect buried volatiles from seasonal thermal effects.

It is important to note that the center panel of Figure 8 shows that the distribution of KS probabilities is biased to low probability events. But a numerical simulation of 1000 stars with uniform randomly chosen brightest-slice rankings f shows that the distribution should be uniform. Applying a KS test to the tail detection KS probability distribution shows that they are inconsistent with a uniform no-activity null hypothesis at the $p = 1.2 \times 10^{-5}$ level, unlike the 1000 stars.

The right panel of Figure 8 shows the angular distribution of the brightest detection segment compared to the distribution for matched stars. Although the distributions for both stars and asteroids are non-uniform, possibly from angular asymmetries in the telescope optics, the bottom panel of the right panel shows that there is a $\sim 2\sigma$ excess of asteroids over stars in the $|\text{PA}_{\text{antisolar}} - \text{PA}_{\text{detec}}| \approx 0^\circ$ direction. *i.e.*, the brightest segment is aligned

with the expected antisolar tail direction. If the sample is restricted to asteroids where the total KS probability is limited to $p < 0.05$ or 0.01 , the excess at zero angle remains at the 1.5 to 2.0σ level.

Thus, barring any systematic biases that we have not already taken into account, we conclude that there is evidence for low level excess directionalized flux around many of the TALCS asteroids and, generalizing further, that main belt asteroids as a class exhibit weak tails or trails. Unfortunately, the evidence is too weak to identify specific asteroids in our sample because none have $p \ll 0.001$. In a sample of 1000 asteroids we expect one object to have $p = 0.001$ by chance so the small KS objects in our TALCS data are not likely candidates.

While we can not select individual objects as candidates for faint MBC tails we can estimate that there is an excess of about 50 objects with faint tails in the TALCS data set. In other words about 5% of the main belt objects in the TALCS data set might exhibit very faint tail or trail activity. If the result is correct it implies that deep images of a large sample of main belt objects acquired in a manner suitable for analysis with our technique would identify low-level activity in main belt objects that otherwise appear asteroidal.

Considering that the known MBCs are transient in their activity our result that $\sim 5\%$ of asteroids are active at *any* time implies that a large fraction of main belt asteroids could be active at *some* time. This result further blurs the traditional distinction between asteroids and comets. On the other hand, we speculate that the mechanism driving the low-level tail activity might not be volatile driven ejection but the result of regolith ejection

due to impacts of small meteoroids. In this case, our results offer constraints on the main belt collisional environment such as the amount of primordial implantation of ice-rich bodies and the fraction of those bodies that were collisionally disrupted (*e.g.*, Bottke *et al.*, 2005; O’Brien & Greenberg, 2005).

5.2. Coma Search

We applied the technique of §4 to fit each of the TALCS objects to an asteroid and coma model and thereby measure the fractional contribution of the putative coma (f_c) to the objects’s flux. Figure 7 shows that most of the resulting f_c were below our sensitivity threshold and effectively consistent with zero. But that sensitivity threshold is sensitive to object-specific parameters such as magnitude, rates of motion, PSFs, and the number of frames used in creating the stacked asteroid.

Thus, for each stacked asteroid the null-image stacking procedure described in §4.1.5 was repeated 50 times per target. In the absence of coma the distribution of h -values for all TALCS objects should be uniform so that after 50 trials no more than $1/50^{th}$ of the TALCS objects should have $h = 1.0$, as discussed in §4.1.5. But instead of the ~ 20 expected objects we found 34. We then subjected those 34 objects to an additional 500 trials after which we expected only ~ 2 TALCS objects with $h = 1.0$ but 8 objects fell into this bin. An additional 5000 trials for each of those 8 objects should have produced zero objects with $h = 1.0$ but 3 remained. In other words, at this stage it appeared that we had identified 3 MBC candidates — the problem was that under detailed visual examination none of these objects displayed any visible coma.

To further investigate the 8 candidates with very high h -values ($h >$

0.998) we divided the set of images for each object in half and separately processed each half with the detection and sensitivity algorithms. If the positive detections remained in each half of the data it would suggest the coma is real. On the other hand, if the coma candidates were not detected in both halves of the data it would suggest either systematic errors in the detection and/or sensitivity algorithms or a transient phenomenon resembling a coma.

Only 1 of the 8 objects had consistently positive coma detections in both halves of its data and, upon visual inspection, it was found to exhibit transient coma-like phenomena in 2 of its 6 images, one in each half. The transient phenomena may be due to it passing over a faint background source. Since we expect real comae to persist over the two weeks spanned by the TALCS observations, and since the signal-to-noise was poor in both the individual and combined frames for this object, we conclude that it is not a MBC candidate. Thus, we have a null result in our search for cometary-like comae in the TALCS survey.

The derived mass loss rates for the TALCS objects are shown in Fig. 7 and it is no surprise that our derived mass loss rates are small and below our sensitivity limits. Typical comets have mass loss rates in the range $10^{-3} \lesssim \dot{M} \lesssim 10^3 \text{ kg}\cdot\text{s}^{-1}$ (*e.g.*, Lamy *et al.*, 2004) with the MBCs falling in the smaller decades of the distribution but still within the range of our sensitivity limit of about $10^{-1} \text{ kg}\cdot\text{s}^{-1}$.

5.3. Upper Limits on MBC Orbit and Size Distributions

Hsieh & Jewitt (2006a) estimated that there is one active MBC for every 300 main belt asteroids based on their Hawaii Trails Survey that focused primarily on Themis family members in the outer main belt. That family and

heliocentric range were of particular interest because the MBCs EP and 176P were already known to be Themis family members and it seemed reasonable to expect that if sub-surface volatiles could survive since the formation of the solar system they would most likely do so in objects that are farther from the Sun. Considering that Hsieh & Jewitt (2006a) did not account for these observational selection effects the 300:1 ratio of main belt asteroids to active MBCs is a lower limit — the ratio could be considerably larger when averaged over the main belt as suggested by Gilbert & Wiegert (2010). However, at face value, the estimate suggests that we should identify ~ 3 MBCs within the TALCS sample since our detection techniques are sensitive to the same cometary activity levels as the known MBCs.

Our null result allows us to set new upper limits on the number distribution of MBCs in absolute magnitude, semimajor axis, eccentricity, and inclination by employing the technique of Moskovitz *et al.* (2008). Given the false-positive rate (F), the differential absolute magnitude distribution of TALCS objects, $n(H)$, the probability of detecting an active MBC within the survey (P_d), and the completeness of the survey as a function of absolute magnitude, $C(H)$, the actual number of MBCs as a function of absolute magnitude is given by:

$$N(H) = \frac{(1 - F) n(H)}{P_d C(H)} . \quad (3)$$

We take $F = 0.001$ ($\sim 1/924$) because of the one questionable detection described at the end of §4.2 though it is functionally equivalent to a zero false-positive rate. Assuming activity levels similar to those previously observed in current MBCs, $P_d = 1.0$ because we have demonstrated that our technique is capable of detecting MBC tails and/or comae at all absolute magnitudes

within our sample.

We used the ASTORB database to obtain the true number distributions ($N(x)$ with $x = a, e, i, H$) of all main belt objects to an absolute magnitude of $H < 14.8$ with $e < 0.4$, $i < 45.0^\circ$, and $2.0 \text{ AU} < a < 3.5 \text{ AU}$. This sample of known asteroids is believed to be complete (Bowell 2007), *i.e.*, all main belt asteroids with $H < 14.8$ are thought to be known. We extrapolated to $H = 21$, the limit of the TALCS sample, using Jedicke *et al.* (2002):

$$N(H) = 0.0059 \times 10^{0.5*H}, \quad 14.8 \leq H < 21. \quad (4)$$

We then derived $C(x)$ by dividing the *observed* number of objects within a given H bin by the total number of objects in that bin.

The unbiased differential number distribution in orbit element x ($x = a, e, i$) is then given by

$$N(x) = \frac{A(H) (1 - F) n(x)}{P_d C(x; H < 21)},$$

where $n(x)$ is the observed number distribution for our TALCS objects and $A(H)$ is a normalization factor computed from the $n(H)$ cumulative number distribution so that the integrated number of TALCS objects in our range of x equals the number in our range of absolute magnitudes. *i.e.*, $A(H) = \int n(x)dx / \int n(H)dH$. $C(x; H < 21)$ is the completeness of the survey as a function of orbit element x for $H < 21$.

Since we found no MBC candidates, $n(x) = 0$ for all x , and Fig. 9 gives the 90% confidence bound limit on the fraction of MBCs using both a standard Poisson framework and a Bayesian framework that accounts for our prior belief of a 1/300 fraction (see Appendix A). The latter method effectively

estimates the MBC fraction by transforming Hsieh & Jewitt (2006a)’s $1/300$ to $1/(300+924)$.

We found that the MBC:MBA ratios for $H < 21.0$ are $\lesssim 1:300$, $\lesssim 1:350$, and $\lesssim 1:500$, for the inner, middle, and outer belt respectively and, averaged over the entire main belt, $\text{MBC:MBA} \lesssim 1:400$. While these limits are numerically not markedly different from (Hsieh & Jewitt 2006a) they are applicable to asteroids to much smaller sizes ($H < 21$ vs. $H < 18$) and were derived from a survey in which we explicitly accounted for observational selection effects. Indeed, Hsieh (2009) recognized the bias in the earlier result and revised the applicability of the MBC:MBA ratio reported in Hsieh & Jewitt (2006a) to low-inclination ($i < 3.0$), ‘km-scale’ MBCs in the outer belt — a population composing only $\sim 10\%$ of the TALCS sample. Hsieh (2009) further re-evaluated the MBC:MBA ratio based on the Hawaii Trails Project (HTP) to be $\sim 1 : 100$.

Gilbert & Wiegert (2009) and Gilbert & Wiegert (2010) used serendipitous detections of asteroids in the CFHT Legacy Survey (CFHTLS, Jones *et al.*, 2006) to identify MBC candidates and measure the MBC:MBA ratio. Since the CFHTLS was not explicitly targeted at identifying MBCs they could correct for the survey’s observational selection effects. They identified one MBC candidate after examining ~ 25000 main belt objects and thus concluded that the MBC:MBA ratio is $\sim 1:25000$ for objects with $H < 16$ (corresponding to objects of more than a few kilometers in diameter). While their value is considerably more stringent than ours it applies to objects ~ 10 times the diameter of our study. It will be interesting to eventually measure the fraction of MBCs as a function of their diameter (or H) in an effort to

provide constraints on thermal models for asteroid evolution but, in order to do so, there will need to be a larger sample study similar to this work or that of Gilbert & Wiegert (2009) and Gilbert & Wiegert (2010).

5.4. Constraints on the Snow Line

One of our original motivations for the TALCS MBC survey was to identify a handful of MBCs in a relatively unbiased survey — at least relatively unbiased in comparison to the HTP of Hsieh & Jewitt (2006a) that specifically targeted regions of the main belt where they thought it likely to discover MBCs. Based on their 1:300 MBC:MBA ratio we optimistically expected to identify a few MBCs in the TALCS data set. With such a set of MBCs in hand we thought it would be possible for the first time to constrain the location of the primordial snow line. *i.e.*, if we found 5 MBCs beyond 2.5 AU and none in the inner belt it could have been strong evidence for a snow line around 2.5 AU. If radial mixing is negligible, then the positions of MBCs could give hints as to the primordial snow line’s location. Having identified zero MBCs in this study we are limited in its application to the location of the snow line but, under a set of simplified assumptions, it is possible to use the locations of the known MBCs to estimate its position.

If the snow line is at semi-major axis a_s and one assumes that 1) *observable* asteroids are evenly distributed in semi-major axis $a \in [A_0, A_1]$ in the asteroid belt (this is in fact the case as shown in fig. 1 for $A_0 \sim 2.2$ and $A_1 \sim 3.2$), and 2) n MBCs have been observed *in an unbiased manner* at semi-major axes a_i , (the unbiased assumption was the motivation for using the TALCS survey), then the probability that a_{\min} , the smallest value of a_i ,

is greater than some value of a is given by the binomial probability:

$$P(a_{\min} > a|a_s) = \begin{cases} \left(\frac{A_1 - a}{A_1 - \max(a_s, A_0)} \right)^n & \text{for } \max(a_s, A_0) < a < A_1 \\ 0 & \text{for } a \geq A_1 \\ 1 & \text{for } a \leq \max(a_s, A_0) \end{cases} \quad (5)$$

Then the differential probability distribution of a_{\min} is given by

$$P(a_{\min}|a_s) = -\frac{dP(a_{\min} > a|a_s)}{da} \Big|_{a=a_{\min}} = \frac{n(A_1 - a_{\min})^{n-1}}{[A_1 - \max(a_s, A_0)]^n}. \quad (6)$$

With no prior expectation for the position of the snow line we simply assume that the probability is constant for finding a_s over some range of a that encompasses the asteroid belt. From the Bayesian perspective, $P(a_{\min}|a_s) \propto P(a_s|a_{\min})$, where a_{\min} is now the innermost observed MBC. Substituting $A_1 = 3.2$ AU and using $a_{\min} = 2.72$ AU from Table 1 as the innermost reliable MBC we obtain a probability for the location of the snow line

$$P(a_s|a_{\min} = 2.72) = \begin{cases} \text{const} \times [3.2 - \max(a_s, 2.2)]^{-6} & \text{for } a_s < 2.72 \\ 0 & \text{otherwise} \end{cases} \quad (7)$$

where the distribution is to be normalized over the plausible range of a_s .

For example, if we believe that any $a_s > 1.5$ AU is equally plausible then from the existing 6 MBCs we derive a nominal 85% confidence that the snow line is outside 2.5 AU. Although this is a weak result given the current ensemble of MBCs it provides a formal mechanism to gauge how the estimate will improve as the MBC sample grows. It is also consistent with conclusions from theoretical models and meteorite studies that in the first few million

years of the solar system's lifetime, the snowline was located inside of ~ 3 AU (*e.g.*, Bertini, 2011, and references therein).

Our naive assumption that the location of *the* snowline was frozen in place during the solar system's formation and might still be present in its primordial location may be of limited utility. Garaud & Lin (2007) and Min *et al.* (2011) calculated that during the formation of the inner solar system the snow line migrated from as little as 0.7 AU to many tens of AU due to changing dust opacities and mass accretion rates in the evolving primordial nebula. Based on their work we might expect a gradient of subsurface water ice abundances across parent body sizes, local number densities, semi-major axes, etc. and, hence, varying MBC activity levels throughout the main belt. In any event, given the lack of knowledge about the evolution of the snowline in proto-solar nebulae, attempts to identify its location or to measure the water gradient in the solar system could provide useful constraints on modelling solar system formation. Perhaps the solar system maintains a record of evolutionary transitions in the proto-solar nebula as the snowline advanced further from the Sun much like glacial moraines leaving permanent records of changes in climate as glaciers recede.

The ability to constrain the location of the primordial snow line in our own solar system is further complicated by recent revelations involving massive re-organization of the distribution of the small bodies during early solar system evolution. The ability to constrain the location of the snow line presupposes that the current distribution of small bodies is mostly representative of their primordial distribution. The observed taxonomic distribution of small bodies progressing from S-complex asteroids in the inner belt, to C-complex in the

middle and outer belt, to D- and P-type asteroids in the Hilda and Jupiter Trojan regions may represent a relic of their original distributions.

Levison *et al.* (2009) have thrown this assumption entirely upside down in suggesting that an inward-then-outward migration of the giant planets caused planetesimals from beyond Neptune’s orbit to scatter into the main belt region, particularly the outer belt. In this scenario objects currently in the main belt do not represent the primordial distribution of planetesimals nor do nearby objects in semi-major axis necessarily have a common origin and formation mechanism. If their work is correct, observations of cometary activity in the main belt could be more useful for mapping out the redistribution of material from the outer solar system than constraining the primordial or contemporary snow line.

6. Summary

1. We developed quantitative techniques for sensitive searches for faint tails and coma around objects that otherwise appear asteroidal. The tail detection algorithm identifies excess flux in pie-sgements of an annulus around an object. The coma detection algorithm fit a detailed PSF model to each candidate object that included a point-like and coma-like PSF component. The tail detection technique could easily identify MBCs at the same activity level as the known MBCs. The coma detection technique is sensitive to mass loss rates that are comparable to the known MBCs as well. Both techniques can be applied to large scale sky survey detections of asteroids.
2. We did not identify any MBC candidates using either technique.

3. Using our null-detection result we set upper limits on the number of MBCs as a function of semimajor axis (AU), eccentricity, inclination, and absolute magnitude.
4. We determine that the MBC:MBA ratio for the entire belt to $H < 21.0$ (~ 150 m in diameter) is $\lesssim 1:400$. For the inner, middle, and outer belts, the ratios at $H < 21.0$ are no greater than 1:300, 1:350, and 1:500, respectively.
5. We presented evidence for extremely low-level tail activity in a surprising fraction of apparently generic main belt asteroids — about 5% of our asteroid sample showed evidence of directional excess flux suggesting that many ‘asteroids’ display low-level activity. If correct, it is not clear whether the activity is due to small scale impacts liberating regolith or to sub-surface volatile activation. It might be possible to identify this activity in targeted deep imaging of many main belt asteroids. It might also be possible to study the production mechanism by breaking a large sample of objects into sets of objects near aphelion and perihelion. If the excess activity is related to the objects’s mean anomaly it could indicate thermal-induced volatile activity.
6. We present a Bayesian argument based on the known distribution of MBCs that suggests with 85% confidence that the contemporary snow line is beyond 2.5 AU.

ACKNOWLEDGEMENTS

This work was made possible with NASA PAST grant NNG06GI46G and was based on observations obtained with MegaPrime/MegaCam, a joint

project of CFHT and CEA/DAPNIA, at the Canada-France-Hawaii Telescope (CFHT) which is operated by the National Research Council (NRC) of Canada, the Institut National des Science de l'Univers of the Centre National de la Recherche Scientifique (CNRS) of France, and the University of Hawaii. This work was partly supported by NASA through the NASA Astrobiology Institute under Cooperative Agreement NNA09DA77A issued through the Office of Space Science. We thank the people of Hawaii for use of their sacred space atop Mauna Kea.

References

- Benford, F. 1938, "The law of anomalous numbers". Proceedings of the American Philosophical Society 78, 551.
- Bertini, I. 2011. Main belt comets: A new class of small bodies in the solar system. Planetary and Space Sci. 59, 365-377.
- Binzel, R. P., Xu, S., & Bus, S. J. 1993. Spectral variations within the Koronis family - Possible implications for the surface colors of Asteroid 243 Ida. Icarus 106, 608-611.
- Birkett, C. M., Green, S. F., Zarnecki, O. C., & Russell, K. S. 1987. Infrared and optical observations of low-activity comets, P/Arend-Rigaux (1984k) and P/Neujmin 1 (1984c). Monthly Notices of the Royal Astronom. Society 225, 285-296.
- Boehnhardt, H., Schulz, R., Tozzi, G. P., Rauer, H., Sekanina, Z. 1996. Comet P/1996 N2 (Elst-Pizarro). IAU Circ. 6495.

- Bottke, W. F., Durda, D. D., Nesvorný, D., Jedicke, R., Morbidelli, A., Vokrouhlický, D., Levison, H. 2005. The fossilized size distribution of the main asteroid belt. *Icarus* 175, 111-140.
- Bowell, E. 2007. Orbits of Minor Planets. *VizieR On-line Data Catalog: B/astorb*.
- Britt, D. T., Yeomans, D., Housen, K., Consolmagno, G., 2002. Asteroid density, porosity, and structure. In: Bottke, W. F., Cellino, A., Paolicchi, P., Binzel, R. P. (Eds.), *Asteroids III*. Univ. of Arizona Press, Tucson, 485-500.
- Capria, M. T., Marchi, S., de Sanctis, M. C., Coradini, A. 2010. The Activity of Main Belt Comets. *Lunar and Planetary Sci. Conf.* 41, 1207
- Carvano, J. M., Mothe-Diniz, T., Lazzaro, D. 2003. Search for relations among a sample of 460 asteroids with featureless spectra. *Icarus* 161, 356-382 .
- Chamberlin, A. B., McFadden, L.-A., Schulz, R., Schleicher, D. G., & Bus, S. J. 1996. 4015 Wilson-Harrington, 2001 Oljato, and 3200 Phaethon: Search for CN Emission. *Icarus* 119, 173-181.
- Cochran, W. D., Cochran, A. L., Barker, E. S. 1986. In: *Asteroids, comets, meteors II – Proc.*, 181-185.
- Denneau, L., Kubica, J., Jedicke, R. 2007. The Pan-STARRS Moving Object Pipeline. *ASP Conference Series* 376, 257-260.

- Drummond, J. D., & Hege, E. K. 1989. In: R. P. Binzel, T. Gehrels, & M. S. Matthews (Eds.), *Asteroids II*, Univ. of Arizona Press, Tucson, pp. 171-191.
- Elst, E. W., Pizarro, O., Pollas, C., Ticha, J., Tichy, M., Moravec, Z., Offutt, W., & Marsden, B. G. 1996. Comet P/1996 N2 (Elst-Pizarro). *IAU Circ.* 6456.
- Fanale, F. P., & Salvail, J. R. 1989. The water regime of asteroid (1) Ceres. *Icarus* 82, 97-110.
- Fernandez, J. A., Gallardo, T., & Brunini, A. 2002. Are there many inactive Jupiter-Family Comets among the Near-Earth Asteroid population? *Icarus* 159, 358-368.
- Fernandez, Y. R., Jewitt, D. C., & Sheppard, S. S. 2005. Albedos of Asteroids in Comet-Like Orbits. *Astronom. J.* 130, 308-318.
- Fukugita, M., Ichikawa, T., Gunn, J. E., Doi, M., Shimasaku, IK., & Schneider, D. P. 1996. The Sloan Digital Sky Survey Photometric System. *Astronom. J.* 111, 1748-1756.
- Garaud, P. & Lin, D. N. C. 2007. The Effect of Internal Dissipation and Surface Irradiation on the Structure of Disks and the Location of the Snow Line around Sun-like Stars. *Astrophys. J.* 654, 606-624.
- Gilbert, A. M. & Wiegert, P. A. 2009. Searching for main-belt comets using Canada-France-Hawaii Telescope Legacy Survey. *Icarus* 201, 714-718.

- Gilbert, A. M. & Wiegert, P. A. 2010. Updated results of a search for main-belt comets using the Canada-France-Hawaii Telescope Legacy Survey. *Icarus* 210, 998-999.
- Grimm, R. E., & McSween, H. Y., Jr. 1989. Water and the thermal evolution of carbonaceous chondrite parent bodies. *Icarus* 82, 244-280.
- Hartmann, W. K., Tholen, D. J., Meech, K., & Cruikshank, D. P. 1990. 2060 Chiron - Colorimetry and cometary behavior. *Icarus* 83, 1-15.
- Hsieh, H. H., Jewitt, D. C., & Fernandez, Y. R. 2004. The Strange Case of 133P/Elst-Pizarro: A Comet among the Asteroids. *Astronom. J.* 127, 2997-3017.
- Hsieh, H. H., & Jewitt, D. D. 2006a. A Population of Comets in the Main Asteroid Belt. *Science* 312, 561-563.
- Hsieh, H. H., & Jewitt, D. C. 2006b. in: D. Lazzaro, S. Ferraz- Mello & J. A. Fernandez (Eds.), *Asteroids, Comets, and Meteors*, Proc. IAU Symposium 229 (Cambridge Univ. Press), 425-437.
- Hsieh, H. H., Jewitt, D., & Ishiguro, M. 2009a. Physical properties of main-belt comet P/2005 U1 (Read). *Astronom. J.* 137, 157-168.
- Hsieh, H. 2009b. The Hawaii trails project: comet-hunting in the main asteroid belt. *Astronom. & Astrophys.* 505, 1297-1310.
- Hsieh, H. H., Jewitt, D., Lacerda, P., Lowry, S. C., & Snodgrass, C. 2010. The return of activity in main-belt comet 133P/elst-Pizarro. *Monthly Notices of the Royal Astronom. Society* 403, 363-377.

- Ipatov, S. I., & Mather, J. C. 2007. In: A. Milani, G. B. Valsecchi, & D. Vokrouhlicky (Eds.), *Near Earth Objects, our Celestial Neighbors: Opportunity and Risk*. IAU Symposium 236 (Cambridge Univ. Press), 55-64.
- Jedicke, R., Denneau, L., Grav, T., Heasley, J., Kubica, J., and PAN-Starrs Team. 2005. Pan-STARRS Moving Object Processing System. *Bulletin of the American Astronomical Society* 37, 1363.
- Jedicke, R., & Metcalfe, T. S. 1998. The Orbital and Absolute Magnitude Distributions of Main Belt Asteroids. *Icarus* 131, 245-260.
- Jedicke, R., Larsen, J., & Spahr, T. 2002. Observational selection effects in asteroid surveys. In: Bottke Jr., W. F., Cellino, A., Paolicchi, P., Binzel, R. (Eds.), *Asteroids III*. Univ. of Arizona Press, Tucson, 71-87.
- Jester, S., et al. 2005, The Sloan Digital Sky Survey View of the Palomar-Green Bright Quasar Survey. *Astronom. J.* 130, 873
- Jewitt, D. C. 2005. A First Look at Damocloids. *Astronom. J.* 129, 530-538.
- Jewitt, D. C., & Meech, K. J. 1987. Surface brightness profiles of 10 comets. *Astrophys. J.* 317, 992-1001.
- Jewitt, D. C., & Luu, J. X. 1989. A CCD portrait of Comet P/Tempel 2. *Astronom. J.* 97, 1766-1790.
- Jewitt, D. 2008. Kuiper Belt and Comets: An Observational Perspective. In: Altwegg, K., Benz, W., & Thomas, N. (Eds.), *Saas- Fee Advanced Course 35: Trans-Neptunian Objects and Comets*. Springer, Berlin, 1-78.

- Jewitt, D., Yang, B., & Haghhighipour, N. 2009. Main-belt comet P/2008 R1 (Garradd). *Astronom. J.* 137, 4313-4321.
- Jewitt, D., Weaver, H., Agarwal, J., Mutchler, M. & Drahus, M. 2010. P/2010 A2: A Newly Disrupted Main Belt Asteroid. *Nature* 467, 817-819.
- Jewitt, D., Weaver, H., Mutchler, M., Larson, S., & Agarwal, J. 2011. Hubble Space Telescope Observations of Main-belt Comet (596) Scheila. *Astrophys. J. Letters* 733, L4.
- Jones, T. D. 1988. An infrared reflectance study of water in outer belt asteroids. Ph.D. Thesis, Univ. of Arizona
- Jones, T. D., Lebofsky, L. A., Lewis, J. S., & Marley, M. S. 1990. The composition and origin of the C, P, and D asteroids - Water as a tracer of thermal evolution in the outer belt. *Icarus* 99, 172-192.
- Jones, *et al.* 2006. The CFEPT Kuiper belt survey: Strategy and presurvey results. *Icarus* 185, 508-522.
- Kanda, Y., Mori, A., Kobayashi, H., & Kawakita, H. 2008. Optical Spectroscopic Observations of Comet 73P/Schwassman-Wachmann 3. *PASJ* 60, 1191-1198.
- Kennedy, G. M., & Kenyon, S. J. 2008. Planet Formation around Stars of Various Masses: The Snow Line and the Frequency of Giant Planets. *Astrophys. J.* 673, 502-512.
- Klacka, J. 1992. Mass distribution in the asteroid belt. In: *Earth Moon, and Planets* 56, 47-52.

- Kleyana, J., Meech, K., & Jewitt, D. 2007. A Search for main Belt Comets with Pan-STARRS 1. *Bulletin of the American Astronom. Society* 38, 227.
- Lamy, P. L., Toth, I., Fernandez, Y. R., Weaver, H. A. 2004. In: M. C. Festou, H. U. Keller, & H. A. Weaver (Eds.), *The sizes, shapes, albedos, and colors of cometary nuclei. Comets II* (Univ. of Arizona Press), 223-264.
- Levison, H. F., Bottke, W. F., Gounelle, M., Morbidelli, A., Nesvorny, D., & Tsiganis, K. 2009. Contamination of the asteroid belt by primordial trans-Neptunian objects. *Nature* 460, 364-366.
- Luu, J. X., & Jewitt, D. C. 1992. High resolution surface brightness profiles of near-earth asteroids. *Icarus* 97, 276-287.
- Magnier, E. A., & Cuillandre, J.-C. 2004. The Elixir System: Data Characterization and Calibration at the Canada-France-Hawaii Telescope. *Publications of the Astronom. Society of the Pacific* 116, 449-464.
- Masiero, J. R., Jedicke, R., Durech, J., Gwyn, S., Denneau, L., Larsen, J. 2009. The Thousand Asteroid Light Curve Survey. *Icarus* 204, 145-171.
- Millis, R. L., A'Hearn, M. F., Campin, S. H. 1988. An investigation of the nucleus and coma of Comet P/Arend-Rigaux. *Astrophys. J.* 324, 1194-1209.
- Min, M., Dullemond, C. P., Kama, M., & Dominik, C. 2011. The Thermal Structure and the Location of the Snow Line in the Protosolar Nebula: Axisymmetric Models with full 3-D Radiative Transfer. *Icarus* 212, 416-426.

- Moreno, F., Licandro, J., Tozzi, G.-P., Ortiz, J. L., Cabrera-Lavers, A., Augusteijn, T., Liimets, T., Lindberg, J. E., Pursimo, T., Rodriguez-Gil, P., Vaduvescu, O. 2010. Water-ice-driven Activity on Main-Belt Comet P/2010 A2 (LINEAR)? *Astrophys. J. Letters* 718, L132-L136.
- Moskovitz, N. A., Jedicke, R., Gaidos, E., Willman, M., Nesvorny, D., Fevig, R., Ivezić, Z. 2008. A Spectroscopically Unique main belt Asteroid: 10537 (1991 RY16). *Astrophys. J.* 682, 57-60.
- Nesvorny, D., Bottke, W. F., Bokrouhlicky, D., Sykes, M., Lien, D. J., Stansberry, J. 2008. Origin of the Near-Ecliptic Circumsolar Dust Band. *Astrophys. J.* 679, 143-146.
- O'Brien, D. P., Greenberg, R. 2005. The collisional and dynamical evolution of the main-belt and NEA size distributions. *Icarus* 178, 179-212.
- Prialnik, D. & Rosenberg, E. D., 2009. Can ice survive in main-belt comets? Long-term evolution models of comet 133P/Elst-Pizarro. *Monthly Notices of the Royal Astronom. Society* 399, L79-L83.
- Sanzovo, G. C., de Almeida, A. A., Misra, A., Torres, R. M., Boice, D. C., & Huebner, W. F. 2001. Mass-loss rates, dust particle sizes, nuclear active areas and minimum nuclear radii of target comets for missions STARDUST and CONTOUR. *Monthly Notices of the Royal Astronom. Society* 326, 825-868.
- Sasselov, D. D., & Lecar, M. 2000. On the Snow Line in Dusty Protoplanetary Disks. *Astrophys. J.* 528, 995-998.

Scott, E. R. D., & Krot, A. N. 2005. Thermal Processing of Silicate Dust in the Solar nebula: Clues from Primitive Chondrite Matrices. *Astrophys. J.* 623, 571-578.

Snodgrass, C., *et al.* 2010. A collision in 2009 as the origin of the debris trail of asteroid P/2010 A2. *Nature* 467, 814-816.

Table 1: Parameters of the seven known MBCs: Object’s name, semimajor axis (a), eccentricity (e), inclination (i), orbital period (P_{orb}), effective diameter (D_e), absolute V magnitude (H_v), and mass loss rate (\dot{M}). Data comes from Hsieh *et al.* (2004), Hsieh & Jewitt (2006a), Jewitt *et al.* (2009), Hsieh *et al.* (2009), Jewitt *et al.* (2010), Moreno *et al.* (2010), and the Minor Planet Center (website: <http://www.minorplanetcenter.net>).

Object	a (AU)	e	i (deg)	P_{orb} (yr)	D_e (km) [†]	H_v	\dot{M} (kg s ⁻¹)
133P/Elst-Pizarro	3.16	0.162	1.39	5.62	3.8	15.9	0.01
238P/Read	3.17	0.253	1.27	5.63	0.6	17.7	0.02
176P/Linear	3.19	0.194	0.24	5.71	4.4	15.1	. . .
P/2008 R1/Garradd	2.73	0.342	15.90	4.50	1.0	$\gtrsim 17.8$	< 1.5
P/2010 A2/Linear ^a	2.29	0.124	5.25	3.47	0.1	21.3	0.1-5
P/2010 R2/La Sagra	3.10	0.154	21.39	5.46	1.5	15.5	. . .
596 Scheila ^a	2.93	0.165	14.66	5.01	113.3	8.90	. . .

Note: [†] Using a geometric albedo of 0.134 characteristic of the outer belt (Jedicke & Metcalfe 1998; Klacka 1992) to calculate the diameter from the published absolute magnitudes.

^a Excess flux from these objects is most likely the result of asteroid collisions rather than recurrent activity typical in comets.

Table 2: Tail fluxes of three known MBCs as a fraction f_T of the central point source and as a median g' magnitude in the brightest photometric segment, illustrated in Fig. 2.

Object	f_T	g'
Elst-Pizarro	0.059	22.87
P/Read	0.086	21.86
176P	0.037	23.08

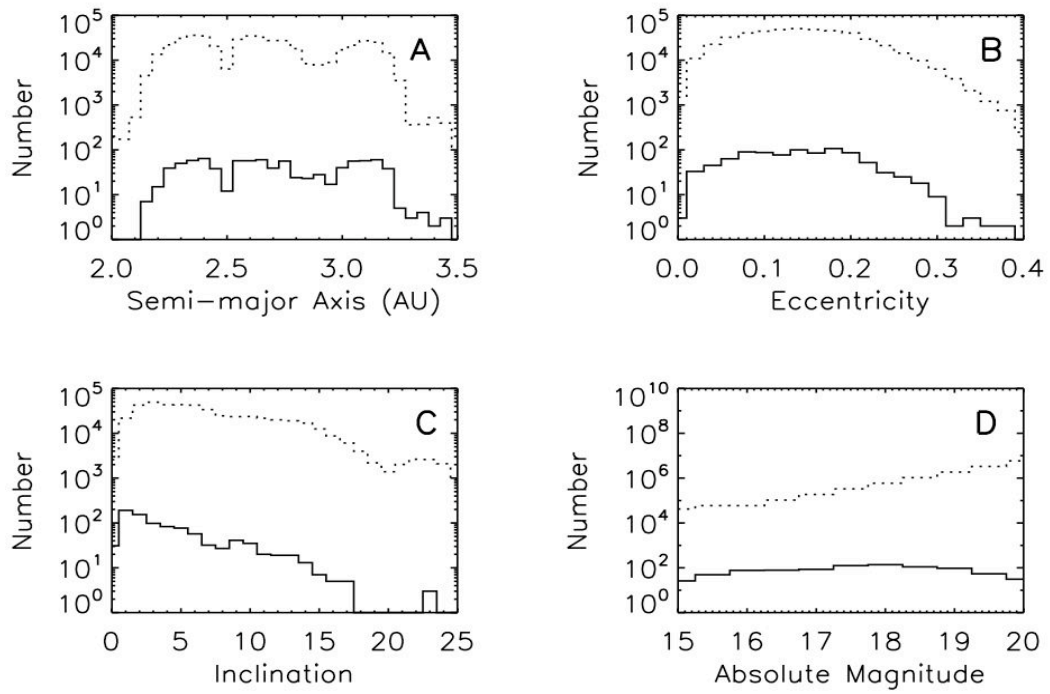


Figure 1: Number distributions of TALCS objects (solid line, Masiero *et al.*, 2009) and those in the ASTORB database (dotted line, Bowell, 2007) as a function of (A) semimajor axis, (B) eccentricity, (C) inclination, and (D) absolute magnitude.

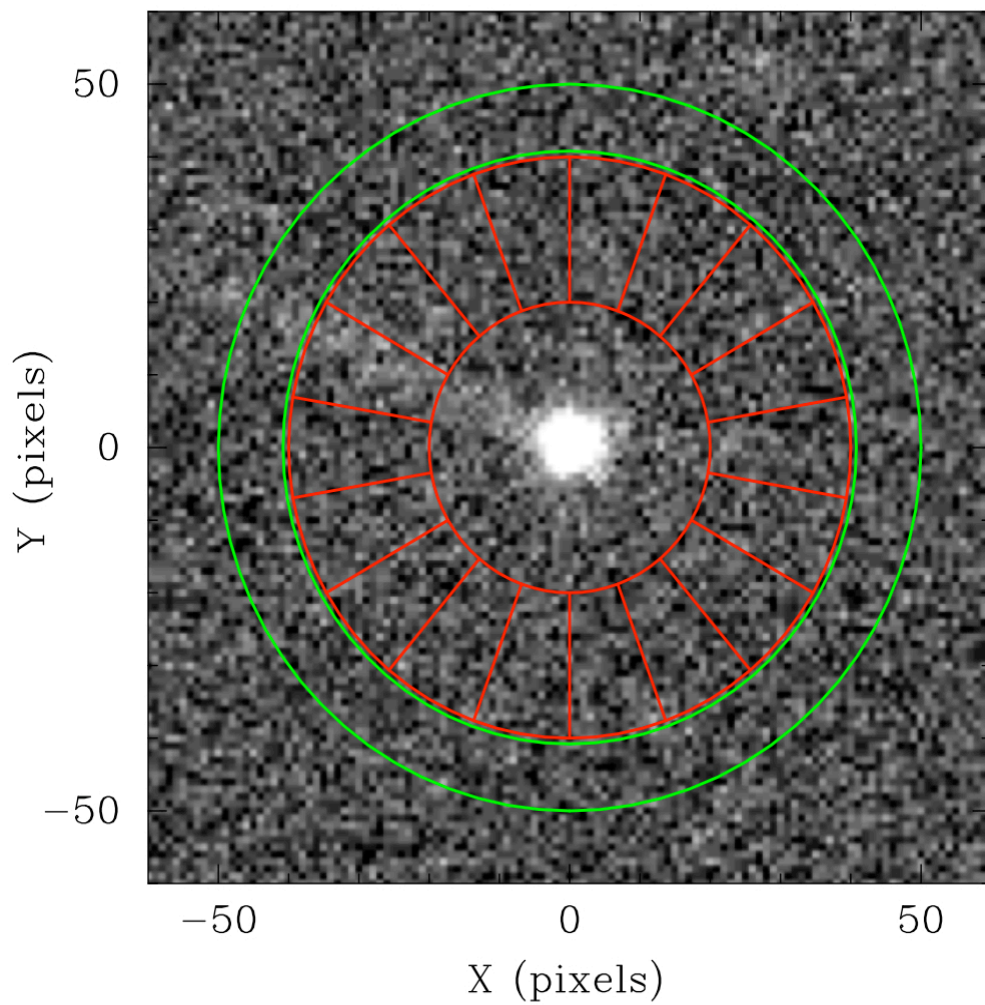


Figure 2: Our scheme for detecting tails or trails around asteroids superimposed on an image of Elst-Pizarro. The red detection annulus is subdivided into 18 polar segments and a tail is detected by recording the brightest segment (here, at approximately 10 o'clock). The green annulus is used to compute a median background which is subtracted before the detection procedure.

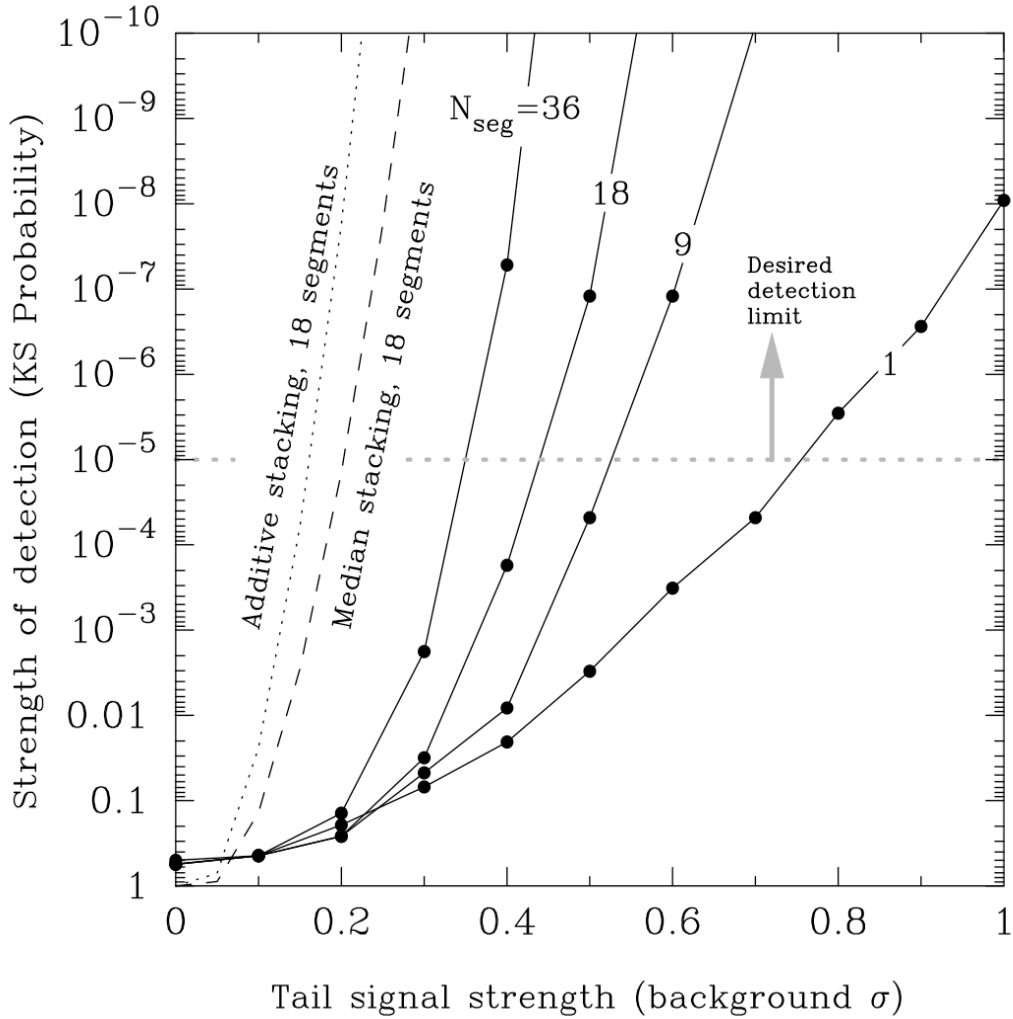


Figure 3: Sensitivity of our segmented annulus tail search method for MBCs. We assume a detection annulus containing Gaussian noise with a known standard deviation and express the signal strength of the tail (horizontal axis) as a fraction of the whole-annulus noise. The technique provides the tail recovery strength (vertical axis; the Kolmogorov Smirnov probability) for each signal strength for the given number of segments N_{seg} . We also show the recovery strength that would be obtained using additive and median image stacking assuming perfect tail alignment and no contamination.

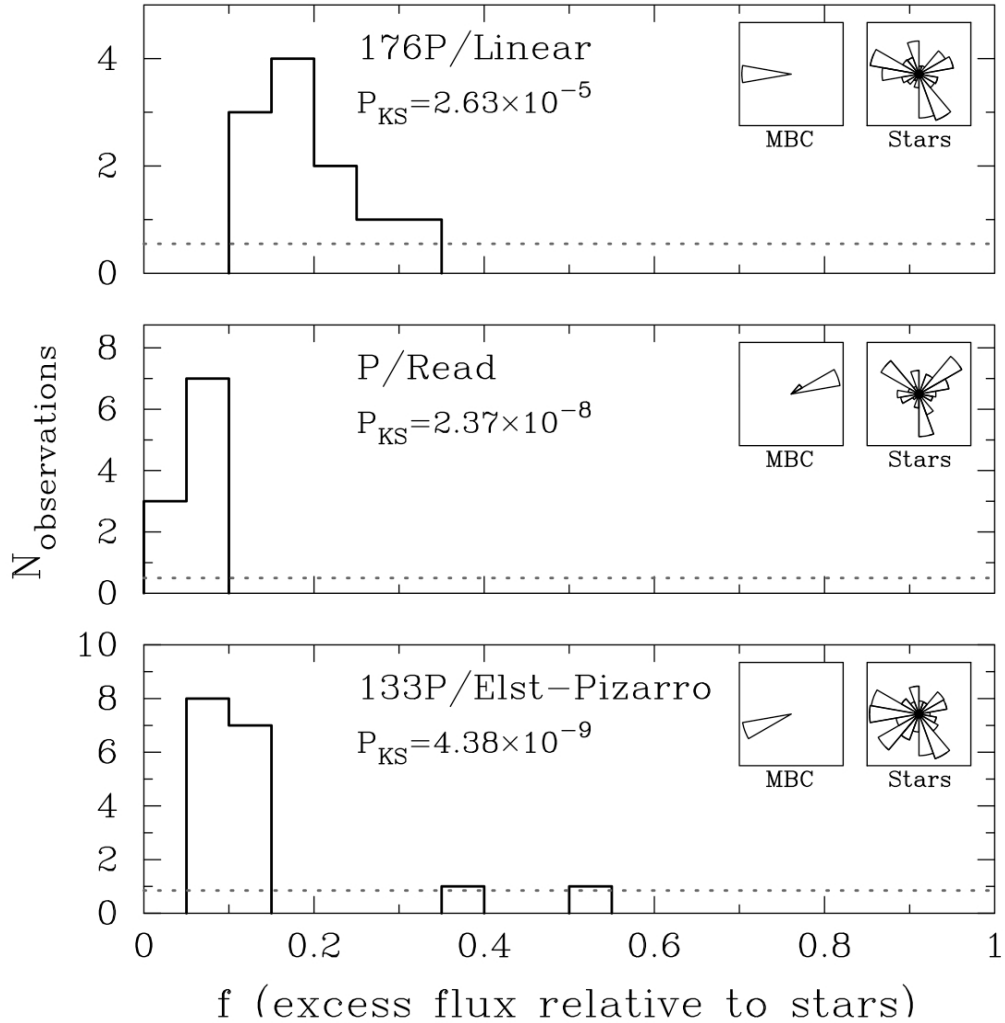


Figure 4: Histogram of the f parameter of excess light relative to field stars (see text) for three known MBCs observed by Hsieh & Jewitt (2006b). The flat dotted line gives the null-hypothesis flat distribution. In each case, the Kolmogorov-Smirnov probability P_{KS} strongly rules out the null hypothesis. The inset boxes are radial histograms depicting the direction of the brightest polar segment for the MBC (left box) and for the calibration stars (right box). The radial length of a polar bin is proportional to the number of exposures in which this bin corresponded to the brightest direction.

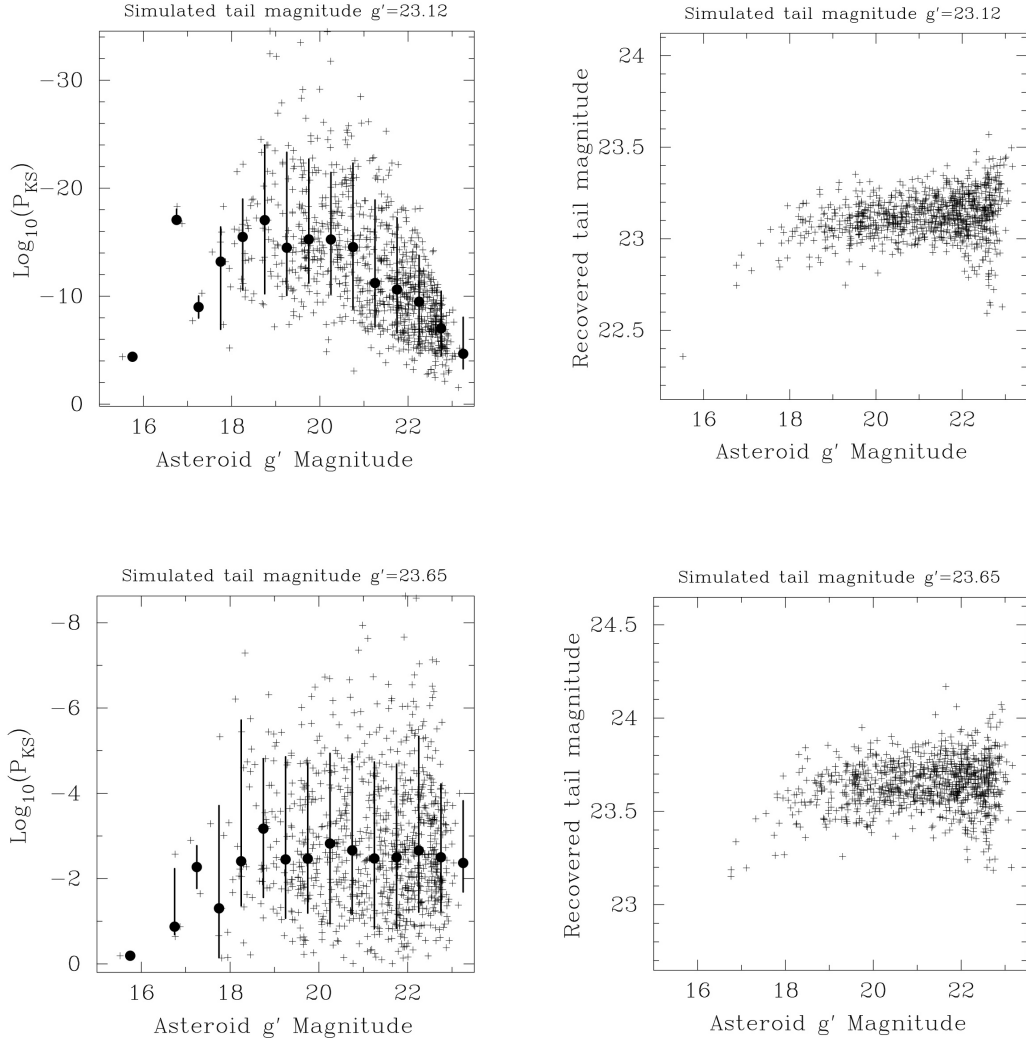


Figure 5: Results of our tail detection algorithm on TALCS data when we added an artificial tail of a fixed magnitude to each asteroid detection. The left column of figures shows the Kolmogorov–Smirnov probability with which a tail is detected; the large point is the median in each half-magnitude bin and the bar is the region containing 90% of points. The right column is the derived magnitude of the recovered tail. The top row of figures provides the results for a simulated tail with a total detection aperture magnitude of $g' = 23.12$, slightly fainter than the faintest known MBC. The bottom row shows the result for a tail 0.5 magnitude fainter (below our detection limit).

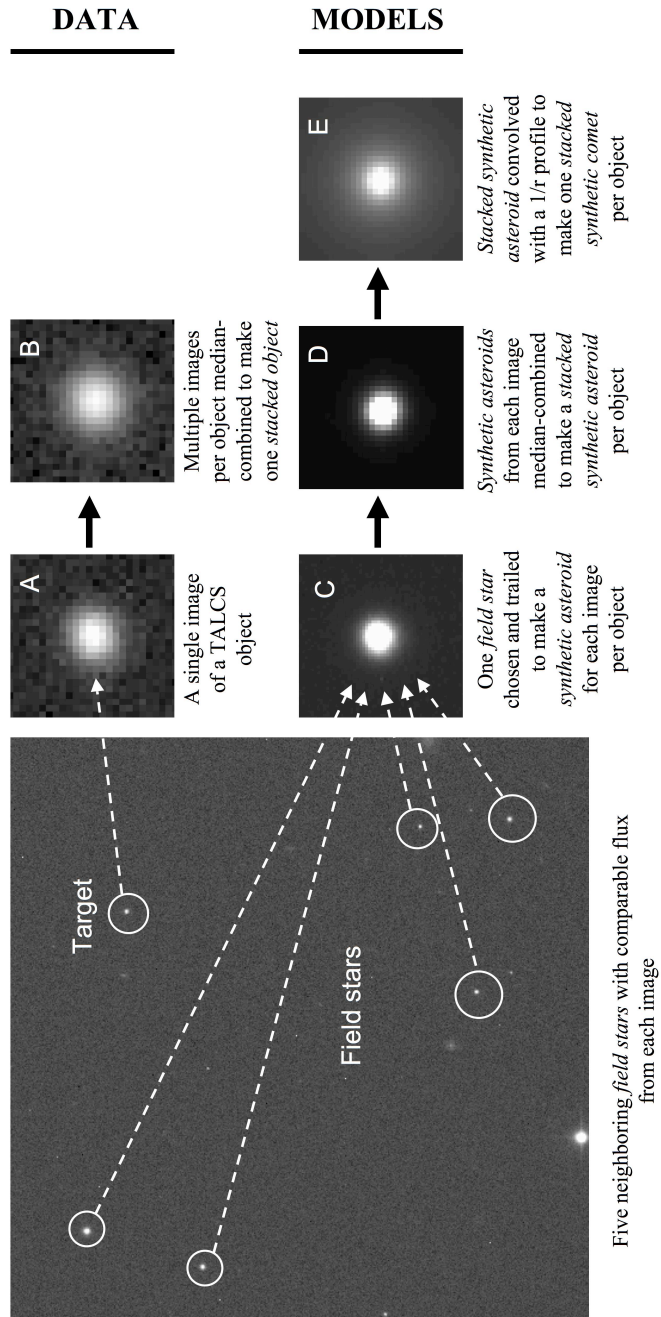


Figure 6: Schematic representation of the production of stacked object images and their accompanying synthetic asteroid and coma models: (A) a single image of a TALCS object; (B) a median-combined image of multiple detections of the same object to produce one stacked object; (C) one field star chosen based upon its similarity to the target in flux, then trailed to make one synthetic asteroid for each image per object; (D) synthetic asteroids median-combined to make one stacked synthetic asteroid per object; (E) each stacked synthetic asteroid is convolved with a $1/r$ profile to make a stacked synthetic comet (coma-only) per object

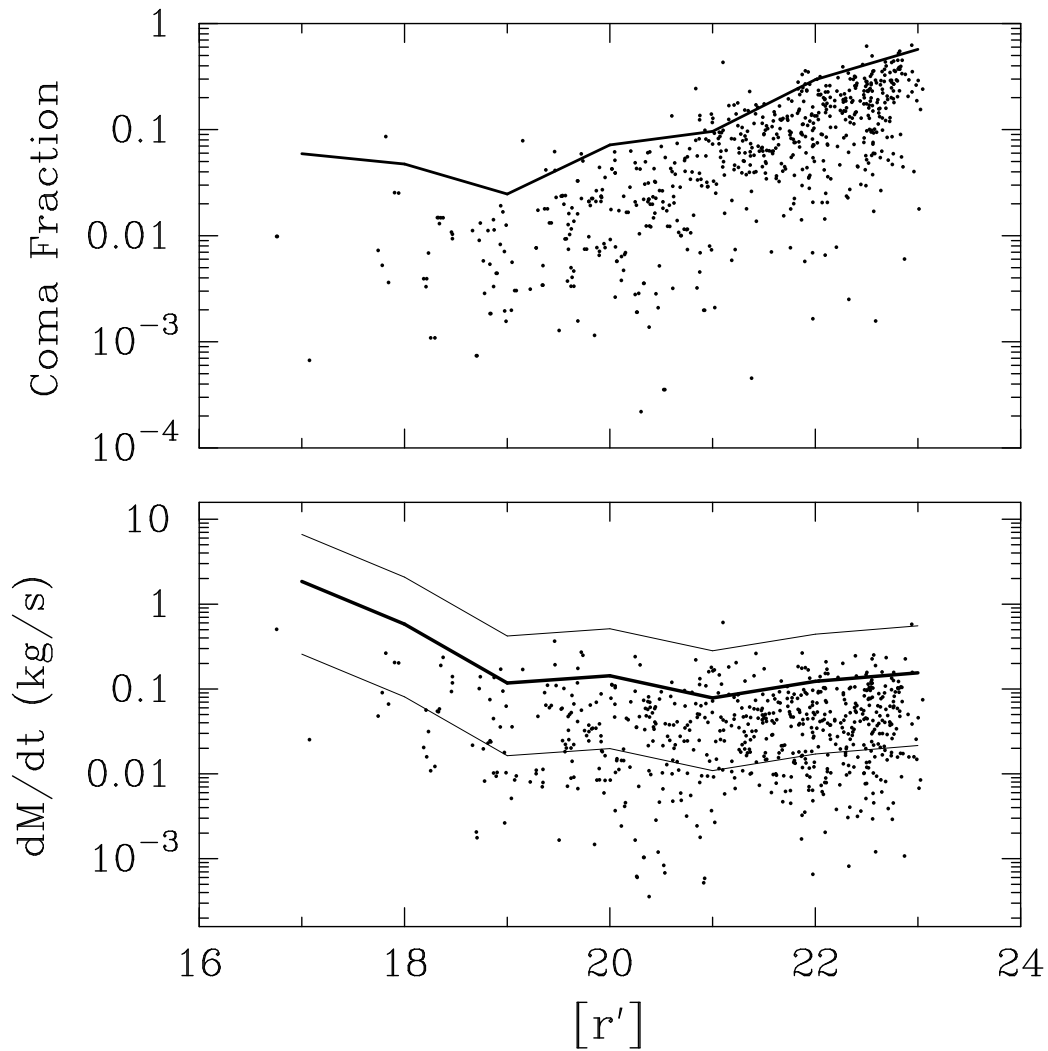


Figure 7: Top: The solid line is the 99.9% confidence bound on the coma fraction f_c for a benchmark asteroid of a given magnitude. Randomly stacking asteroids yields an f_c above the solid line only 0.1% of the time. The data points represent the derived values for the TALCS asteroids. Bottom: A conversion of the f_c in the top panel into a mass loss rate. From top to bottom the solid lines represent placing the benchmark asteroid at heliocentric distances of $R = 3.6, 2.6, 1.6$ AU.

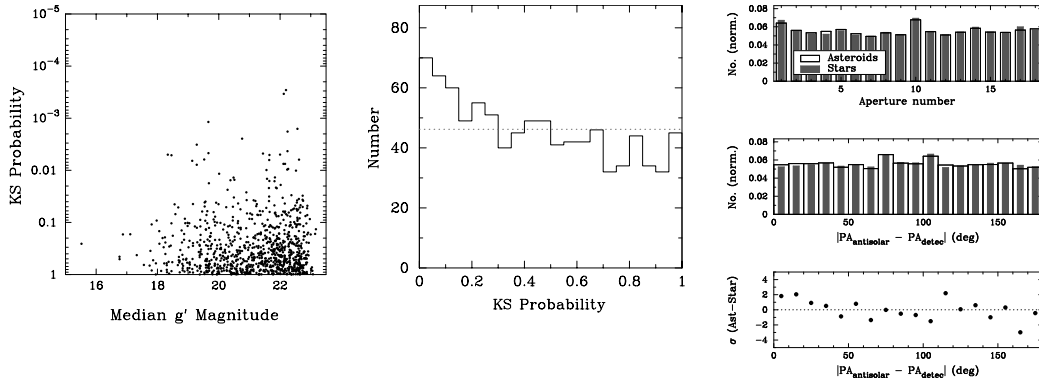


Figure 8: Left: Tail detection significance for all asteroids in the TALCS data set. The vertical axis is the Kolmogorov-Smirnov (KS) probability as in Figure 3. Center: The distribution of KS probabilities from the left panel. The horizontal dotted line represents the expected distribution under the assumption that there is no tail or trail activity. Right: The angular distribution of the brightest detection segment as a function of angular aperture number (top) and deviation from the expected anti-solar tail direction (center) for asteroids and similar stars (± 0.1 mag) on the same chip; and (bottom) the significance in σ of the excess asteroid counts in each angular bin compared to the stars. It is evident from the stars that the angular distribution is non-uniform and dominated by systematics (top and center), but there is $\sim 2\sigma$ excess in asteroids for the two bins closest to the antisolar direction once the systematics are removed using the stars.

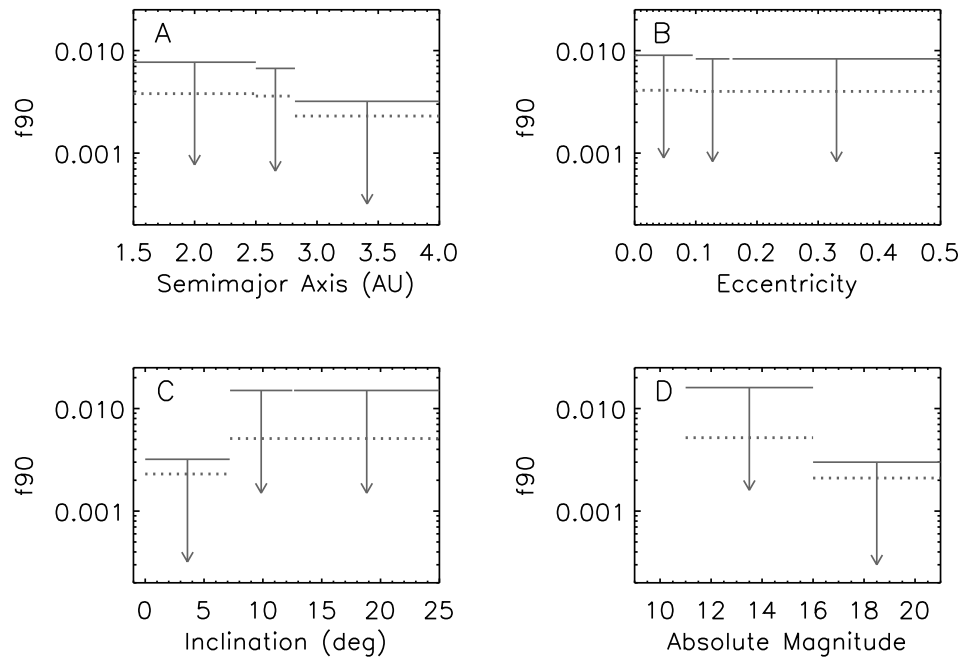


Figure 9: Poisson (solid) and Bayesian (dotted) 90% confidence limits on MBC number distributions as a function of (a) semi-major axis, (b) eccentricity, (c) inclination, and (d) absolute magnitude. See Appendix A for a detailed discussion of the Poisson vs. Bayesian approach.

Appendix A. Bayesian and frequentist statistics for zero detections

In this work we present constraints on the true (unbiased) rate of MBC activity using observations that yielded zero detections in M observations. Such an extrapolation is inherently problematic because it depends strongly on assumptions of the incidence f of MBCs or, more formally, on the Bayesian prior $P(f)$.

Appendix A.1. A frequentist approach

The customary Poisson frequentist model begins with the fact that the probability of observing n MBCs given an expected number $\langle n \rangle$ is

$$P_{\text{Pois}}(n) = \frac{\langle n \rangle^n e^{-\langle n \rangle}}{n!} = \frac{(fCM)^n e^{-fCM}}{n!} \quad (\text{A.1})$$

where in the rightmost component we have defined the survey completeness (sensitivity) as $C \in [0, 1]$ and identified $\langle n \rangle = fCM$. Under the frequentist paradigm, f_{90} , the 90% upper confidence limit on f is given by the implicit equation:

$$0.9 = \frac{\int_0^{f_{90}} P_{\text{Pois}}(n) df}{\int_0^1 P_{\text{Pois}}(n) df} \quad (\text{A.2})$$

For $n = 0$

$$f_{90} = -(CM)^{-1} \ln(1 - 0.9) \quad (\text{A.3})$$

However, this model has several undesirable features. First, it assumes that when $n = 0$ MBCs are found the expected number is 1^3 irrespective

³because for $n = 0$, $P(f) = CM e^{-fCM}$; then $\langle n \rangle = CM \langle f \rangle$ and $\langle f \rangle = \int_0^1 f P(f) df \approx (CM)^{-1}$.

of the size of the sample. *e.g.*, If we observe only 10 asteroids and our completeness is $C = 1$ then the analysis yields $f_{90} = 0.23$ — implying that we are 90% confident that $< 23\%$ of asteroids are MBCs. On the other hand, the alternative interpretation is that we are 10% confident that MBCs represent more than 23% of asteroids but this is easily seen to be wrong because of prior knowledge from other surveys.

Next, the statistical implications are altered by binning the data. If we observe $M = 1000$ asteroids and $n = 0$ MBCs we would compute $f_{90} = 0.0023$ for the entire sample, meaning that we have 10% confidence that a typical sample of asteroids contains 2.3 or more MBCs. However, if were to divide the sample into 100 semi-major axis bins of 10 asteroids each and re-apply the statistics we would assign $f_{90} = 0.23$ to each bin. *i.e.*, that each bin of 10 asteroids has a 10% chance of containing more than 2.3 MBCs, an expected MBC count that far exceeds what was obtained when the data were contained in a single bin.

Both examples show the formal Poissonian f_{90} does not represent a genuine confidence limit (in the sense of betting odds) because we overestimate the 10% probability assigned to $f > f_{90}$. In the first case, this happens because we assign a prior probability that ignores previous knowlege. In the second case we pretend that each bin is independent when we know that a failure to find an MBC in 99 bins means it is very unlikely to find one in the 100th bin.

A resolution to the problems inherent to the Poissonian frequentist approach is a Bayesian approach to the question.

Appendix A.2. A Bayesian approach

A Bayesian approach remedies at least the first flaw described above at the cost of ‘contaminating’ our confidence intervals with knowledge from other surveys. Indeed, the above Poisson approach was simply a Bayesian method with a constant prior on f .

We begin our analysis by assuming a prior for f

$$P(f) = \begin{cases} [-f \log(f_0)]^{-1} & \text{for } f \in [f_0, 1] \\ 0 & \text{elsewhere} \end{cases} \quad (\text{A.4})$$

where $f_0 \ll 1$ is the smallest allowed value of f and is assumed to approach 0. The f^{-1} prior is the basis of Benford’s law (Benford 1938) and implies that f is equally likely to reside in each decade of magnitude within the range of interest. By allowing $f_0 \rightarrow 0$ we assert an initial belief that MBCs are extremely unlikely to exist.

Next, we modify our prior using the study of Hsieh & Jewitt (2006a) (hence HJ06) who found one MBC in a targeted survey of $M_{HJ} = 300$ asteroids. Bayes’ theorem informs us that an experimental result E modifies our prior belief for $P(f)$ according to

$$P(f|E) = \frac{P(E|f) \times P(f)}{P(E)} \quad (\text{A.5})$$

Here E is an experiment consisting of an observation of some number of MBCs n in a given sample of M asteroids. Assuming completeness or survey sensitivity $C \in [0, 1]$ gives the binomial probability distribution:

$$P(E|f) = P(n|f; C, M) = \frac{M!}{n!(M-n)!} (Cf)^n (1-Cf)^{M-n} \quad (\text{A.6})$$

where we use the notation that items after a semicolon are fixed parameters. Then the probability of observing experimental result E , or n objects, is

$$P(E) = P(n; C, M) = \int_0^1 P(f)P(n|f, C, M) df \quad (\text{A.7})$$

Thus the posterior probability of f given experiment E is obtained by combining Equations A.4, A.5, A.6 and A.7

$$\begin{aligned} P(f|E) &= P(f|n; C, M) \\ &= \frac{(Cf)^n(1 - Cf)^{M-n} \times f^{-1}}{\int_{f_0}^1 (Cf)^n(1 - Cf)^{M-n} \times f^{-1} df} \end{aligned} \quad (\text{A.8})$$

where the normalization given by $-\log(f_0)$ and the factorial terms have cancelled. The denominator of equation A.8 is a constant normalization term and for $n > 0$ we may allow it to reach the limiting value $f_0 = 0$ without encountering a singularity.

Using HJ06's result of $n = 1$ the posterior probability is

$$P(f|E_{HJ}) = M_{HJ} \times (1 - f)^{M_{HJ}-1}. \quad (\text{A.9})$$

This probability is relatively constant for $f \lesssim 1/M_{HJ}$ compared to the original divergent prior $P(f) \propto f^{-1}$ and we have assumed $C_{HJ} = 1$ because the observations of HJ06 are deeper than ours. This posterior is effectively the distribution of f for objects that could have been detected by HJ06 and might be detected by us after adjusting for our completeness, C .

Finally, we may use $P(f|E_{HJ})$ as a Bayesian prior for our TALCS study where we find n MBCs in M asteroids:

$$P(f|E_{\text{TALCS}}) = \frac{(Cf)^n(1 - Cf)^{M-n-1}P(f|E_{HJ})}{\int_0^1 P(f|E_{HJ})(Cf)^n(1 - Cf)^{M-n-1} df} \quad (\text{A.10})$$

$$= \frac{(Cf)^n(1 - Cf)^{M-n-1}(1 - f)^{M_{HJ}}}{\int_0^1 (Cf)^n(1 - Cf)^{M-n-1}(1 - f)^{M_{HJ}} df} \quad (\text{A.11})$$

To compute uncertainties it is necessary to integrate $P(f|E_{\text{TALCS}})$ up to the desired confidence boundary. For the case $C = 1$, Equation A.10 simplifies to a ratio of incomplete beta functions.

Although the Bayesian approach addresses the problem of inconsistency with prior knowledge it does not resolve the binning difficulty. As smaller bins of new data are considered the recovered MBC fraction defaults to the Bayesian prior. In fact, the absence of MBCs in neighboring bins should provide information on the number expected in a particular bin because there is no reason to believe that the bins are completely independent. For instance, we do not genuinely believe that the MBC fraction for semimajor axis $a \in [2.1, 2.2]$ is given by $f \sim M_{\text{HJ}}^{-2}$ when we observed zero MBCs out of a thousand asteroids at other values of a . A correct treatment would require assigning a prior probability to the independence of the bins.

Appendix A.3. Conclusion

Because of the problems discussed above, one cannot view the formal bound f_{90} as a simple “betting” confidence and any interpretation of the limits must be in light of the caveats of this Appendix. The simplest interpretation may be the most reliable: if we use the HJ06 result as a Bayesian prior and consider our sample as a whole, we arrive at

$$P(f|E_{\text{TALCS}}) = (M_{\text{HJ}} + M_{\text{TALCS}}) \times (1 - f)^{M_{\text{HJ}} + M_{\text{TALCS}} - 1} \quad (\text{A.12})$$

which is identical to a single combined experiment that discovered one MBC.